Giant Domain Walls and Intrinsic Heterogeneity in

214 Cuprate Superconductors

Evie Ladbrook¹, Jon Wright², Mark S. Senn^{1*}

¹Department of Chemistry, University of Warwick, Coventry, CV4 7AL, United Kingdom.

²European Synchrotron Radiation Facility, Grenoble, France.

*Corresponding author(s). E-mail(s): m.senn@warwick.ac.uk;

Abstract

The intricate interplay of structural, charge and spin orders in layered cuprates leads to emergent phenomena, most notably high-temperature superconductivity. However, there is growing awareness that both the structure and electronic ordering that underpin them are not fully homogeneous. Here, we employ scanning three-dimensional X-ray diffraction to spatially resolve structural distortions in ${\rm La_{1.675}Eu_{0.2}Sr_{0.125}CuO_4}$, a prototypical system that exhibits a strong competition between superconductivity and charge density wave order, across its low-temperature orthorhombic to tetragonal phase transition. We uncover two forms of intrinsic microstructural heterogeneity: at 300 K, we reveal remarkably wide tetragonal-like domain wall regions within the nominally orthorhombic crystal structure, and, upon cooling to 100 K, a fine microstructure of orthorhombic-like stripes embedded within the tetragonal matrix emerges. This spatially resolved view directly defines the microstructural architecture of phase coexistence in this system, demonstrating how structural distortions generate intrinsic heterogeneity that shapes the balance between superconductivity and charge density wave order as constrained by the restrictive orthorhombic and tetragonal structures, offering a pathway to control correlated phenomena.

1 Main

The physical properties of materials are intricately tied to their microstructure, where spatial variations in symmetry, composition and electronic order can stabilise behaviours absent in the bulk. Inhomogeneities such as domain walls can become active elements, hosting properties like enhanced conductivity [1], polarity [2] or ferroelectricity [3]. In high-temperature superconducting cuprates, the interplay of structural distortions with charge, spin and superconducting orders results in phenomena like charge stripes [4], nematicity [5] and filamentary superconductivity [6]. Yet, the contribution of the underlying microstructure remains poorly understood. Here we use scanning three-dimensional X-ray diffraction to directly visualise the structural distortions in a bulk single crystal of La_{1.675}Eu_{0.2}Sr_{0.125}CuO₄. We reveal unusually broad (approx. 150 nm) tetragonal domain wall-like regions within the low-temperature orthorhombic phase, and, upon cooling, a contrasting microstructure of fine orthorhombic-like stripes embedded within the low-temperature tetragonal phase. These findings show that these systems are intrinsically heterogenous and critically shapes the balance between superconductivity and charge density wave order.

Inhomogeneities, whether structural, electronic or chemical, can drive the separation of materials into distinct phases on the nanometre to micrometre scale, with significant effects on the properties [7, 8]. This is most notably observed in the manganites, where the colossal change in resistance under applied magnetic fields is believed to be linked to the percolation of a ferromagnetic conducting phase within a charge ordered antiferromagnetic insulating matrix [9]. High-temperature superconducting cuprates also exhibit rich phase diagrams with competing orders. We investigated $La_{1.675}Eu_{0.2}Sr_{0.125}CuO_4$ (LESCO), a prototypical 1/8 doping level cuprate characterised by its suppression in T_C [10, 11]. Critically, LESCO appears to exhibit signatures of structural coexistence between the low-temperature orthorhombic (LTO) and low-temperature tetragonal (LTT) phases over a broad temperature range [12],

reminiscent of electronic phase separation observed in other highly correlated systems. While these signatures are also evident in other 1/8 doped cuprates, and notably absent in the isostructural band insulator La_2MgO_4 [13], prevailing interpretations and theories often assume a homogeneous structural state underpins both superconducting and charge density wave (CDW) order.

At room temperature, LESCO adopts the LTO (Bmab) phase, characterised by rotations of the CuO₆ octahedra about the [100] axis, as shown in Fig. 1a. This distortion transforms as $X_3^+(a;0)$, with respect to the high-temperature tetragonal (HTT, I4/mmm, F4/mmm in the basis of LTO) phase. Upon cooling to approximately 160 K, LESCO undergoes a first-order phase transition from LTO to an LTT $(P4_2/ncm)$ phase, in which the octahedra rotate about [110] and [110], with alternating layers rotating in opposite senses. This is described by $X_3^+(a;a)$. The absence of a groupsubgroup relationship between LTO and LTT necessarily means the phase transition is first-order and there is a region of phase coexistence. However, the persistence of this down to at least as low as 10 K in LESCO and isostructural ${\rm La_{1.875}Ba_{0.125}CuO_4}$ (LBCO) suggests a coupling to electronic phase separation related to an intrinsic competition between superconductivity and CDW order at this doping level. While CDW order is believed to suppress bulk superconductivity [4], in-plane superconducting correlations may persist [14, 15]. In the LTO phase, charge stripe alignment across layers enables bulk superconducting coherence, but in the LTT phase, the octahedral rotations pin charge stripes and induce a 90° rotation between adjacent layers, frustrating interlayer Josephson coupling [16, 17]. Similar frustrations may occur at structural domain walls, where the sense of the octahedral rotations reverses, inducing corresponding charge stripe rotations. Therefore, a detailed understanding of the microstructure at the domain-level appears essential for accurately measuring and controlling superconductivity.

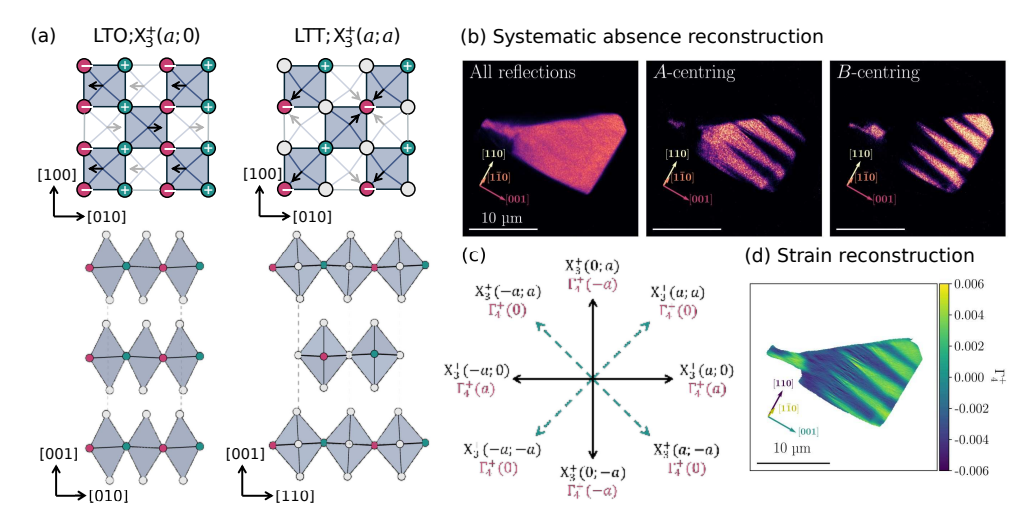


Fig. 1 (a) Representation of the LTO (left) and LTT (right) structures, with A-site cation omitted for clarity. Oxygens are shown in teal and magenta indicating whether they are above and below the ${\rm CuO_2}$ planes, respectively. In LTO, the sense of the distortion propagates along [010], with all layers aligned. In LTT, the sense of the distortion propagates along alternating diagonals, with a 90° rotation, from [110] to [110], between adjacent layers. (b) 300 K reconstruction of the sample from all reflection and filtered by A- and B-centred systematic absences, revealing twin domains. (c) Order parameter map indicating ${\rm X}_3^+$ propagation direction with black as LTO and teal as LTT (d) 300 K strain reconstruction based on ${\rm \Gamma}_4^+$ showing strong correlations with systematic absence map. Axes are given with respect to the LTO/LTT basis.

To directly resolve this complex microstructure, we used scanning three-dimensional X-ray diffraction [18, 19], allowing spatially resolved characterisation of LTO- and LTT-like structural domains in the bulk from 300 to 100 K. This method contrasts techniques like transmission electron microscopy (TEM), which typically only provide surface-sensitive information, as it instead offers a cross section through the bulk. Using the full diffraction signal indexed on a $5.35 \times 5.35 \times 13.2$ Å unit cell, the shape of the slice through the crystal can be tomographically reconstructed (Fig. 1b). A more insightful view of the underlying twin domain structure emerges by performing the reconstruction using only a subset of reflections. The two orthorhombic twin domains, related by a fourfold rotation about the c-axis, have different systematic absence conditions relative to the lattice used to index all observed reflections. They correspond to either an A- or B-centred lattice, characterised by general reflection conditions k+l= even or h+l= even, respectively. This distinction arises from

the orientation of the octahedral tilting, as illustrated in Fig 1c. This clearly resolves a micron-scale domain structure composed of interlocking A- or B-centred regions, orientated parallel to [001] and perpendicular to [110] and [1 $\bar{1}$ 0], likely forming continuous sheets in the out-of-plane direction. The [001] direction is approximately 2° out of the plane of the image which may account for the triangular shape of the domains if the sheets are not of a constant thickness throughout the crystal.

As the LTT structure emerging at lower temperature lacks general systematic absence conditions to differentiate it from the LTO domains, contrast was instead achieved through variation in the ferroelastic strain, Γ_4^+ , that acts as a secondary order parameter of the octahedral tilting, X_3^+ . Iterative reconstructions based on the spatial distribution of the local average unit cell parameters [20] (further details provided in the Methods) recovered Fig. 1d. The strong correlation between the systematic absence reconstruction (from reflection intensities, Fig. 1b) and the strain reconstruction (from peak positions, Fig. 1d) provides robust validation of our approach. Given its superior resolution (10^{-4} [21]) relative to systematic intensity errors, we focus our subsequent analysis on strain reconstructions. This provides a level of detail generally hard to achieve with techniques like TEM over such large length scales.

Fig. 2 shows the spatial variation of the symmetry adapted strain with respect to the I4/mmm aristotype and associated histograms at 300 K.

Among these, Γ_4^+ is unique in exhibiting a pronounced, stripe-like pattern, directly aligned with the orthorhombic twin structure. In contrast, the other strain modes show only subtle spatial deviations, most notably in $\Gamma_1^+(2)$, which corresponds to an elongation of c, and $\Gamma_5^+(b)$, associated with a shearing between c and the ab plane. We note that the small spatial variation in $\Gamma_5^+(b)$, most likely arising from strain localised at the domain walls, may provide an explanation for the apparent subtle monoclinic distortion recently reported in LBCO [22]. This distinction is reinforced by the corresponding histograms. Γ_4^+ demonstrates a bimodal distribution offset from

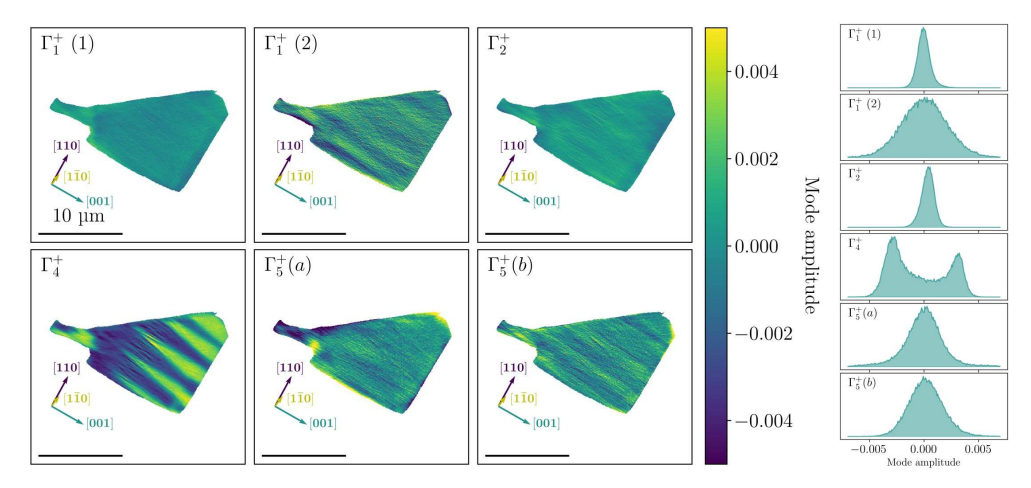


Fig. 2 Spatially resolved maps and associated histograms of symmetry-adapted strain modes at 300 K. Note the bimodal distribution of Γ_4^+ , unique in capturing the twin domain structure. $\Gamma_1^+(1)$ corresponds to an in-plane symmetric expansion/contraction, while $\Gamma_1^+(2)$ is a uniform strain along c. Γ_2^+ is an in-plane shear strain. Γ_4^+ is the orthorhombic strain. $\Gamma_5^+(a)$ and $\Gamma_5^+(b)$ describe shear strains between the ab plane and c axis.

zero, reflecting the alternating strain across the twin domains. By comparison, the other strain modes show uniform distributions centred around zero, consistent with the stable or weakly varying distortions. These can be well modelled by a single pseudo-Voigt distribution and would, for example, give rise to anisotropic peak broadening due to sample microstrain in powder XRD. This symmetry-based decomposition reveals that Γ_4^+ uniquely captures the structural signature of the octahedral tilting.

The evolution of Γ_4^+ upon cooling (Fig. 3a-b) provides critical insight into the LTO/LTT transition. From 300 to 140 K, the A-centred LTO domain gradually dominates to accommodate the growing ferroelastic strain, leading to a marked asymmetry in the Γ_4^+ distribution (Fig. 3b). However, before the minority domain is fully consumed, the increasing magnitude of X_3^+ , inherently coupled to Γ_4^+ , triggers the first-order transition to LTT [13]. This behaviour, occurring near the critical octahedral tilting amplitude for T_C , is not a coincidence but instead suggests a structural basis underlying the suppression of superconductivity in the composition-doping phase diagram of this material class [12]. At 120 and 100 K, the overall micro-scale variation in

 Γ_4^+ appears to be lost, consistent with a more homogenous LTT structure. However, analysis of the absolute strain magnitude $|\Gamma_4^+|$ (Fig. 3c) uncovers crucial sub-micron variation at all temperatures, reminiscent of tweed domain structures [23].

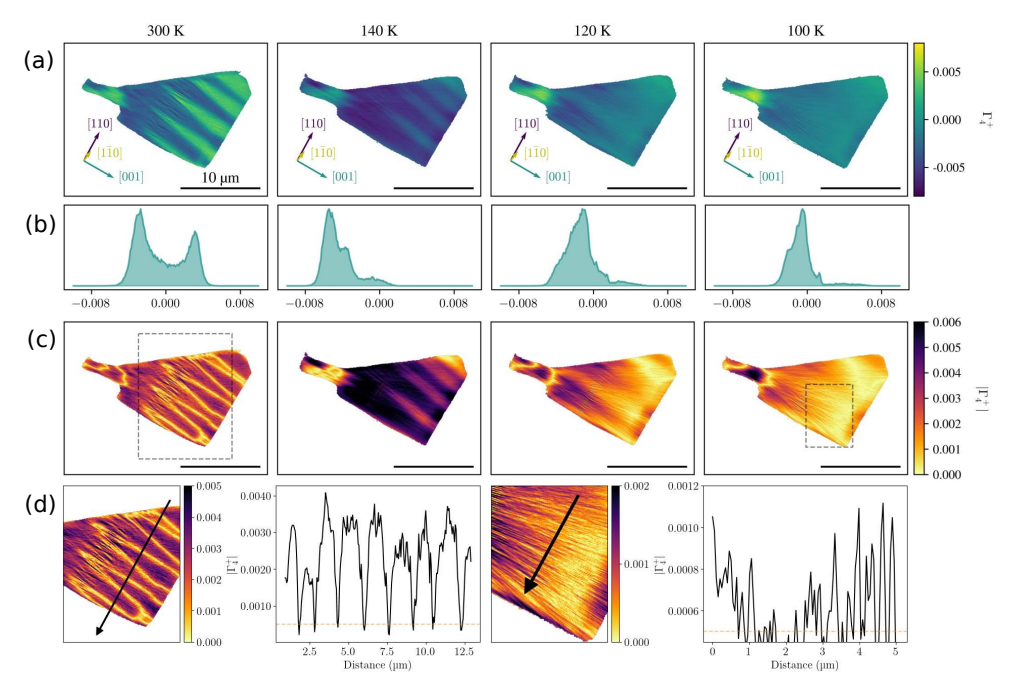


Fig. 3 (a) Spatially resolved maps of Γ_4^+ at 300 K, 140 K, 120 K and 100 K, illustrating the temperature evolution of the structural domains. (b) Histograms of Γ_4^+ at corresponding temperatures, showing the transition from bimodal at 300 K to a more homogenous but still asymmetric distribution at 100 K. (c) Maps of the absolute strain magnitude $|\Gamma_4^+|$ with (d) showing enhanced maps and line profiles, revealing broad LTT-like features within the LTO phase at 300 K and subtle LTO-like filaments within the LTT phase at 100 K. The spatial resolution of our reconstructions is at least 70 nm. see Methods.

At 300 K, within the nominally LTO phase, our $|\Gamma_4^+|$ strain map reveals unusually wide, domain wall-like regions with near-zero strain. These features are not atomic-scale defects, but extended regions approximately 150 nm thick and separated by $0.5-2~\mu m$ (see Fig. S6/Table S1). This length scale is orders of magnitude larger than typical ferroelastic or ferroelectric domain walls. Consequently, these structures challenge the more conventional understanding of what we would view as a domain wall or as microscopic coexisting phases with distinct symmetry. Instead, the observed walls

are effectively extended LTT-like regions coexisting within an LTO matrix [24, 25]. Their substantial thickness would give rise to coherent scattering signals observable as distinct phases in conventional XRD, offering a natural explanation for the phase coexistence reported in LESCO and related cuprates [12, 26, 27].

Considering Fig. 1c, we construct a microscopic model for the evolution of the tilt order parameter across these domains. The strain profile shows a smooth transition from positive to negative Γ_4^+ through extended regions where Γ_4^+ approaches zero. This behaviour is consistent with a continuous rotation of the tilt, for example a sequence such as $X_3^+(a;0)|X_3^+(a;a)|X_3^+(0;a)$. A microscopic (crystallographic) picture for these possible domain evolutions is given in the SI (Fig. S5). The presence of local tetragonal character is consistent with early structural studies on related cuprates [28–31] which suggest that ideally sharp orthorhombic twin walls are unlikely because they would require the CuO₆ octahedra to tilt abruptly in orthogonal directions, resulting in a high interfacial energy. Instead, extended boundaries are expected, in which the tilt pattern gradually transitions from orthorhombic to tetragonal at the wall centre. TEM measurements on LBCO estimated the width of these tetragonal regions to be around 100 Å, while neutron diffraction indicated larger values of a few hundred Å based on superstructure peak broadening [28]. Consistently, Landau-type free-energy models for LBCO predict that the central region of such walls should adopt LTT-like character rather than revert to the HTT phase [32].

Anomalously wide and structurally coherent walls have been increasingly recognised in ferroic materials, but not widely discussed in superconducting materials. In $Ca_3Ti_2O_7$, infrared nano-spectroscopy revealed 60 - 100 nm wide ferroelastic walls, attributed to a gradual rotation of the octahedral tilt and rotation order parameters [33]. Similarly, Néel-like ferroelectric domain walls, where the polarisation rotates rather than vanishes, have been predicted and observed in systems such as $BaTiO_3$

[34, 35]. These examples support a broader understanding of wide domain boundaries as intrinsic structural features that can serve as functionally active elements [36, 37].

At 100 K, within the CDW phase, the microstructure evolves markedly. Deviations from ideal tetragonal symmetry emerge as fine stripe-like orthorhombic features on the 100-200 nm scale, repeating with a similar periodicity. These may be interpreted as nanoscale inclusions of the LTO phase embedded within the LTT matrix, likely forming to minimise the elastic energy associated with antiphase boundaries related to the octahedral tilt orientation $(X_3^+(a;a)/X_3^+(-a;a))$. While similar behaviour has been reported previously in LBCO, where electron microscopy revealed a fine mixture of domains with orthorhombic and tetragonal character with sizes of ≥ 300 Å that persisted well below the LTO/LTT transition to 10 K [38, 39], the likely significance of this with respect to interpreting the bulk properties of these materials has apparently been overlooked in the preceding three decades. Additionally, their regular spatial distribution and morphology, along with the lack of correlation between Γ_4^+ and $\Gamma_1^+(1)$, confirms that they are not artefacts from chemical inhomogeneities but rather reflect an intrinsic and robust microstructure.

From the observed strain profiles, only negative Γ_4^+ is present at 100 K which constrains the domain configurations. The absence of positive Γ_4^+ implies that the domain sequences must be of the form $X_3^+(-a;a)|X_3^+(0;a)|X_3^+(a;a)$ or $X_3^+(-a;-a)|X_3^+(0;-a)|X_3^+(a;-a)$. These LTO-like inclusions will locally disrupt the CDW-stabilising LTT tilt pattern, constraining the CDW correlation length and explaining why it does not fully saturate in LESCO [40]. Such fine structural heterogeneity therefore actively shapes CDW order and may provide filamentary pathways for localised or lower-dimensional superconductivity [41–43]. While recent work has highlighted the crucial role of structural domain walls, particularly those originating from the LTO phase, in defining the formation and stability of CDW order in cuprates [44], until now, a detailed picture of the relevant microstructure has been missing.

The resulting fine structural heterogeneity not only coexists with CDW order but actively influences it, potentially offering a framework for the microscopic coexistence of CDW order, superconductivity and even antiferromagnetic order [45, 46]. Such intricate microstructural variations highlights the need for local probe techniques capable of resolving electronic behaviour at similar length scales. Although conductive atomic force microscopy (cAFM) is promising in this respect for certain materials, we find that anion migration in LESCO currently prevents reliable interpretation, leaving the development of robust local probe methodologies an open challenge.

Our findings reveal an intrinsic, temperature-dependent structural heterogeneity in LESCO that evolves between 300 K and 100 K. This indicates that the global energy minimum is reached only through a complex spatial evolution of distortions that are intertwined with, and underpin, the electronic phase transitions. This picture is likely to be relevant to a broad range of electronic materials and significant for other layered perovskites, such as superconductors Sr_2RuO_4 [47] and $La_3Ni_2O_7$ [48, 49], which also exhibit complex structural phase transitions driven by octahedral tilting, suggesting they may harbour similar heterostructures influencing their physical properties.

Ultimately, our direct visualisation of these microstructural heterogeneities within bulk samples prompts a re-evaluation of how material structure is conceptualised. Increasingly, such variations in the field of ferroic materials are seen not as simple interfaces but as potentially functional components [50]. This raises a philosophical question: should we consider these extensive heterogeneities as distinct coexisting phases, or should we instead hold a more holistic view of material structure in which the intricate interplay of continuous and discrete structural variations governs macroscopic properties? New experimental techniques, such as the use of scanning three-dimensional X-ray diffraction that we have demonstrated here, will be instrumental in capturing the high-resolution structural data necessary to confront this challenge, enabling a more nuanced understanding of complex materials.

2 Methods

2.1 3DXRD measurement

Single crystal samples were selected from the same growth batch as in [12]. A single crystal of approximate dimensions $15 \times 20 \times 20$ µm was secured on a MiTeGen cryoloop using a UV-curing resin. This prevents the crystal from moving during data collection. 3DXRD measurements were performed at the ID11 beamline at the ESRF using a beam energy of 43.5 keV. The beam was focused to 120 nm in size. Sinogram scans were taken as the sample was alternately rotated forwards and backwards over 180° with a step size of 0.05° . The diffractometer was translated with a step size of 50 nm over a 26 µm range. Scans took around 2 hours. Measurements were taken at 300, 140, 120 and 100 K. All measurements were performed at the same nominal position in z, though slight variations may result from thermal contraction of the sample holder with cooling.

2.2 Data processing

All data were processed using the ImageD11 software package [51]. The raw sinogram data were obtained at each temperature. Individual diffraction spots were identified, corrected [52] and converted to reciprocal space coordinates using instrument calibration from a silicon single crystal. Peaks were indexed using an averaged orthorhombic unit cell for 300 and 140 K and a tetragonal unit cell for 120 and 100 K. (hkl) indices were then assigned to each observed reflection.

Reconstruction of the crystal shape, as shown in Fig. 1b, proceeded using tomographic back projection of the peak intensities versus diffractometer y-coordinate. The reconstruction was enhanced using the Maximum Likelihood Expectation Maximisation (MLEM) algorithm [53]. Local variations in the lattice parameters within the crystal were fit using an adaptation of the tomographic algorithm recently described by Henningsson and Hall [20] and implemented using the ASTRA toolbox [54]. The

local lattice parameters within each voxel were refined by fitting the observed peak positions to the metric tensor equation from powder diffraction:

$$\frac{1}{d^2} = Ah^2 + Bk^2 + Cl^2 + Dkl + Ehl + Fhk \tag{1}$$

An initially uniform 2D image of the metric tensor elements (A - F) was forward projected to generate a sinogram by weighting each of the six layers according to the grain shape reconstruction. The resulting $1/d^2$ values for each hkl projection in the 2D sinogram were then compared to observed peak positions. The fit was optimised using a linear least-squares method (L-BFGS algorithm in SciPy) to minimise the sum of squared differences between calculated and observed $1/d^2$ values. This refinement procedure applied no symmetry constraints or regularisation, enabling an unbiased reconstruction of local lattice distortions. Unlike conventional strain tensor approaches, this method does not require an explicit reference 'd-zero' lattice, as the refinement directly fits the metric tensor elements.

The refined metric tensor elements were used to calculate the local lattice basis vectors for each voxel. These were then used to compute symmetry-adapted strain modes with respect to the I4/mmm aristotype structure, where $a=b\neq c$ and $\alpha=\beta=\gamma=90^{\circ}$. Reference values of a and c were defined as the average lattice parameters across all voxels at each temperature. Further details are provided in the Supplementary Information (S1 with schematic diagrams of strain modes in Fig. S1).

The intrinsic spatial resolution of the reconstructions in our experiment is established in the Supplementary Information (Fig. S8 and Table S2) by studying a ferroic material, $Ca_{2.15}Sr_{0.85}Ti_2O_7$, where the existence of giant domain walls have previously been evidenced in the related system $Ca_3Ti_2O_7$ [33]. We find our spatial resolution to be consistently between 30-70 nm at a strain-resolution of 2×10^{-4} . The strain resolution of ID11 in the setup used for the present experiment is better than 2×10^{-4} .

Additionally, studies on scanning-based imaging techniques have shown that oversampling can enhance the spatial resolution beyond the limit set by the beam size [55, 56]. Fig. S10 shows the reciprocal space reconstruction generated from the raw diffraction data, where diffraction spots that must originate from three distinct domains (two LTO and the LTT domains) are clearly resolved.

Acknowledgements. We thank Lauren Cane and Stephen Hayden for synthesis of the sample and Philipp Fahler-Münzer and Donald Evans for test cAFM measurements. E. L. thanks the University of Warwick for a PhD studentship through the Warwick Centre for Doctoral Training in Analytical Science. M. S. S. acknowledges the Royal Society for a fellowship (UF160265 & URF\R\231012) for funding. We acknowledge the European Synchrotron Radiation Facility (ESRF) for provision of synchrotron radiation facilities at beamline ID11 under proposal number HC-5590.

Declarations

Data availability. The raw experimental 3DXRD data are available at doi.org/10.15151/ESRF-ES-1734554406 [57].

References

- [1] Seidel, J. et al. Conduction at domain walls in oxide multiferroics. Nature Materials 8, 229–234 (2009).
- [2] Zubko, P., Catalan, G., Buckley, A., Welche, P. R. L. & Scott, J. F. Strain-Gradient-Induced Polarization in SrTiO₃ Single Crystals. *Physical Review Letters* 99, 167601 (2007).
- [3] Tao, A. et al. Ferroelectric polarization and magnetic structure at domain walls in a multiferroic film. Nature Communications 15, 6099 (2024).

- [4] Tranquada, J. M., Sternlieb, B. J., Axe, J. D., Nakamura, Y. & Uchida, S. Evidence for stripe correlations of spins and holes in copper oxide superconductors. Nature 375, 561–563 (1995).
- [5] Hinkov, V. et al. Electronic Liquid Crystal State in the High-Temperature Superconductor YBa₂Cu₃O_{6.45}. Science 319, 597–600 (2008).
- [6] Phillips, J. C. Filamentary microstructure and linear temperature dependence of normal state transport in optimized high temperature-superconductors. Proceedings of the National Academy of Sciences 94, 12771–12775 (1997).
- [7] Dagotto, E. Complexity in Strongly Correlated Electronic Systems. Science 309, 257–262 (2005).
- [8] Campi, G. et al. Inhomogeneity of charge-density-wave order and quenched disorder in a high- T_C superconductor. Nature 525, 359–362 (2015).
- [9] Uehara, M., Mori, S., Chen, C. H. & Cheong, S.-W. Percolative phase separation underlies colossal magnetoresistance in mixed-valent manganites. *Nature* 399, 560–563 (1999).
- [10] Moodenbaugh, A. R., Xu, Y., Suenaga, M., Folkerts, T. J. & Shelton, R. N. Superconducting properties of La_{2-x}Ba_xCuO₄. Physical Review B 38, 4596–4600 (1988).
- [11] Fink, J. et al. Phase diagram of charge order in La_{1.8-x}Eu_{0.2}Sr_xCuO₄ from resonant soft x-ray diffraction. Physical Review B 83, 092503 (2011).
- [12] Tidey, J. P. et al. Pronounced interplay between intrinsic phase-coexistence and octahedral tilt magnitude in hole-doped lanthanum cuprates. Scientific Reports 12, 14343 (2022).

- [13] Tidey, J. P. et al. Structural origins of the low-temperature orthorhombic to low-temperature tetragonal phase transition in high- T_C cuprates. Physical Review B 106, 085112 (2022).
- [14] Hanaguri, T. et al. A 'checkerboard' electronic crystal state in lightly hole-doped Ca_{2-x}Na_xCuO₂Cl₂. Nature 430, 1001–1005 (2004).
- [15] Berg, E. et al. Dynamical Layer Decoupling in a Stripe-Ordered High- T_C Superconductor. Physical Review Letters **99**, 127003 (2007).
- [16] Fujita, M., Goka, H., Yamada, K., Tranquada, J. M. & Regnault, L. P. Stripe order, depinning, and fluctuations in La_{1.875}Ba_{0.125}CuO₄ and La_{1.875}Ba_{0.075}Sr_{0.050}CuO₄. Physical Review B 70, 104517 (2004).
- [17] Sears, J. et al. Structure of charge density waves in La_{1.875}Ba_{0.125}CuO₄. Physical Review B 107, 115125 (2023).
- [18] Poulsen, H. F. et al. Applications of high-energy synchrotron radiation for structural studies of polycrystalline materials. Journal of Synchrotron Radiation 4, 147–154 (1997).
- [19] Wright, J., Giacobbe, C. & Majkut, M. New opportunities at the Materials Science Beamline at ESRF to exploit high energy nano-focus X-ray beams. Current Opinion in Solid State and Materials Science 24, 100818 (2020).
- [20] Henningsson, A. & Hall, S. A. An efficient system matrix factorization method for scanning diffraction based strain tensor tomography. Acta Crystallographica. Section A, Foundations and Advances 79, 542–549 (2023).
- [21] Borbély, A., Renversade, L. & Kenesei, P. On the calibration of high-energy X-ray diffraction setups. II. Assessing the rotation axis and residual strains. *Journal*

- of Applied Crystallography 47, 1585–1595 (2014).
- [22] Hu, X. et al. Charge density waves and pinning by lattice anisotropy in 214 cuprates. Phys. Rev. B 111, 064504 (2025).
- [23] Salje, E. & Parlinski, K. Microstructures in high T_c superconductors. Superconductor Science and Technology 4, 93 (1991).
- [24] Croft, T. P., Lester, C., Senn, M. S., Bombardi, A. & Hayden, S. M. Charge density wave fluctuations in La_{2-x}Sr_xCuO₄ and their competition with superconductivity. *Phys. Rev. B* 89, 224513 (2014).
- [25] Wang, Q. et al. High-Temperature Charge-Stripe Correlations in La_{1.675}Eu_{0.2}Sr_{0.125}CuO₄. Physical Review Letters 124, 187002 (2020).
- [26] Axe, J. D. et al. Structural phase transformations and superconductivity in La_{2-x}Ba_xCuO₄. Physical Review Letters 62, 2751–2754 (1989).
- [27] Crawford, M. K. et al. Lattice instabilities and the effect of copper-oxygensheet distortions on superconductivity in doped La₂CuO₄. Physical Review B 44, 7749–7752 (1991).
- [28] Zhu, Y. et al. Tetragonal-Orthorhombic Structural Modulation at Low Temperature in La_{2-x}Ba_xCuO₄. Physical Review Letters **73**, 3026–3029 (1994).
- [29] Horibe, Y., Inoue, Y. & Koyama, Y. Direct observation of dynamic local structure in $\text{La}_{2-x}\text{Sr}_x\text{CuO}_4$ around x=0.12. Physical Review B **61**, 11922–11927 (2000).
- [30] Braden, M. et al. Characterization and structural analysis of twinned $\text{La}_{2-x}\text{Sr}_x\text{CuO}_{4\pm delta}$ crystals by neutron diffraction. Physica C: Superconductivity 191, 455–468 (1992).

- [31] Horibe, Y., Inoue, Y. & Koyama, K. Microstructure and Tc-suppression in Lacuprates. Physica C: Superconductivity 282-287, 1071-1072 (1997).
- [32] Cai, Z.-X. & Welch, D. O. Theory on the Structure of Twin Boundaries in La_{2-x}Ba_xCuO₄. MRS Online Proceedings Library (OPL) **357**, 453 (1994).
- [33] Smith, K. A. et al. Infrared nano-spectroscopy of ferroelastic domain walls in hybrid improper ferroelectric Ca₃Ti₂O₇. Nature Communications 10, 5235 (2019).
- [34] Yudin, P. V., Gureev, M. Y., Sluka, T., Tagantsev, A. K. & Setter, N. Anomalously thick domain walls in ferroelectrics. *Physical Review B* 91, 060102 (2015).
- [35] Lee, M. H. et al. Hidden Antipolar Order Parameter and Entangled Neel-Type Charged Domain Walls in Hybrid Improper Ferroelectrics. Physical Review Letters 119, 157601 (2017).
- [36] Xia, W. et al. Giant Domain Wall Anomalous Hall Effect in a Layered Antiferromagnet EuAl₂Si₂. Physical Review Letters 133, 216602 (2024).
- [37] Aird, A. & Salje, E. K. H. Sheet superconductivity in twin walls: experimental evidence of WO_{3-x}. Journal of Physics: Condensed Matter 10, L377 (1998).
- [38] Chen, C. H., Cheong, S.-W., Werder, D. J., Cooper, A. S. & Rupp, L. W. Low temperature microstructure and phase transitions in La_{2-x}Sr_xCuO₄ and La_{2-x}Ba_xCuO₄. *Physica C: Superconductivity* **175**, 301–309 (1991).
- [39] Chen, C. H., Werder, D. J., Cheong, S.-W. & Takagi, H. Micro-twin and antiphase domain boundaries in the orthorhombic phase of La_{2-x}(Sr, Ba)_xCuO₄. *Physica* C: Superconductivity 183, 121–129 (1991).

- [40] Lee, S. et al. Generic character of charge and spin density waves in superconducting cuprates. Proceedings of the National Academy of Sciences 119, e2119429119 (2022).
- [41] Gofryk, K. et al. Local Inhomogeneity and Filamentary Superconductivity in Pr-Doped CaFe₂As₂. Physical Review Letters 112, 047005 (2014).
- [42] Xiao, H. et al. Evidence for filamentary superconductivity nucleated at antiphase domain walls in antiferromagnetic CaFe₂As₂. Physical Review B 85, 024530 (2012).
- [43] Venditti, G. & Caprara, S. Charge-Density Waves vs. Superconductivity: Some Results and Future Perspectives. Condensed Matter 8, 54 (2023).
- [44] Chen, X. M. et al. Charge density wave memory in a cuprate superconductor. Nature Communications 10, 1435 (2019).
- [45] Pratt, D. K. et al. Coexistence of competing antiferromagnetic and superconducting phases in the underdoped Ba(Fe_{0.953}Co_{0.047})₂As₂ compound using x-ray and neutron scattering techniques. *Phys. Rev. Lett.* **103**, 087001 (2009).
- [46] Choi, J. et al. Spatially inhomogeneous competition between superconductivity and the charge density wave in YBa₂Cu₃O_{6.67}. Nature Communications 11, 990 (2020).
- [47] Maeno, Y., Ikeda, A. & Mattoni, G. Thirty years of puzzling superconductivity in Sr₂RuO₄. Nature Physics **20**, 1712–1718 (2024).
- [48] Ko, E. K. et al. Signatures of ambient pressure superconductivity in thin film La₃Ni₂O₇. Nature 638, 935–940 (2025).

- [49] Puphal, P. et al. Unconventional Crystal Structure of the High-Pressure Superconductor La₃Ni₂O₇. Physical Review Letters **133**, 146002 (2024).
- [50] Salje, E. K. H. Multiferroic Domain Boundaries as Active Memory Devices: Trajectories Towards Domain Boundary Engineering. ChemPhysChem 11, 940–950 (2010).
- [51] Wright, J. P. FABLE-3DXRD/ImageD11 (2025). URL https://github.com/ FABLE-3DXRD/ImageD11.
- [52] Wright, J. P., Giacobbe, C. & Lawrence Bright, E. Using Powder Diffraction Patterns to Calibrate the Module Geometry of a Pixel Detector. Crystals 12, 255 (2022).
- [53] Bonnin, A., Wright, J. P., Tucoulou, R. & Palancher, H. Impurity precipitation in atomized particles evidenced by nano x-ray diffraction computed tomography. *Applied Physics Letters* 105, 084103 (2014).
- [54] van Aarle, W. et al. Fast and flexible X-ray tomography using the ASTRA toolbox. Optics Express 24, 25129–25147 (2016).
- [55] Zhang, Y., Lun, M. C., Li, C. & Zhou, Z. Method for improving the spatial resolution of narrow x-ray beam-based x-ray luminescence computed tomography imaging. *Journal of Biomedical Optics* 24, 086002 (2019).
- [56] Kim, J., Hayashi, Y. & Yabashi, M. The emergence of super-resolution beyond the probe size in scanning 3DXRD microscopy. *Journal of Synchrotron Radiation* 30, 1108–1113 (2023).
- [57] HC-5590 (2027). European Synchrotron Radiation Facility. doi.org/10.15151/ESRF-ES-1734554406.